Constitutive Modeling of Reinforced Concrete and Prestressed Concrete Structures Strengthened by Fiber Reinforced Plastics

H.-T. Hu, F.-M. Lin, H.-T. Liu, Y.-F. Huang and T.-C. Pan
Department of Civil Engineering, National Cheng Kung University
Tainan, Taiwan 701, R.O.C.

ABSTRACT

A batch of constitutive models for steel reinforcing bar, prestressing tendon, concrete and fiber-reinforced plastic are proposed for the nonlinear finite element analysis of reinforced concrete structures, prestressed concrete structures, reinforced concrete structures strengthened by fiber reinforced plastics and prestressed concrete structures strengthened by fiber reinforced plastics. These material models have been tested against series of experimental data and good agreements have been obtained, which justifies the validity and the usefulness of the proposed nonlinear constitutive models.

Keywords: Reinforced concrete, Prestressed concrete, Strengthened, Fiber reinforced plastics.

1. Introduction

Due to lightweight, high strength and good fatigue and corrosion properties, fiber-reinforced plastics (FRP) have been intensively used in the repair and strengthening of aerospace structures [1-4]. Though, the study of using FRP to strengthen concrete structures just started in the 90's [5-16], the technology is currently widely used for both reinforced concrete structures [17-25] as well as prestressed concrete structures [26-33].

To study the behavior of reinforced concrete and prestressed concrete structures strengthened by FRP, the fundamental step is to understand the nonlinear behavior of the constitutive materials such as steel reinforcing bar, prestressing tendon, concrete and FRP, separately. The nonlinear behavior of concrete such as concrete cracking, tension stiffening, shear retention, concrete plasticity, yielding of reinforcing steel and yielding of prestressing tendon have been extensively studied by various researchers and numerous proper constitutive laws have been proposed [34-40]. However, in the literature, most studies of reinforced concrete structures strengthened by FRP have assumed that the behavior of FRP is linear. It is well known that unidirectional fibrous composites exhibit severe nonlinearity in their in-plane shear stress-strain relations [41]. In addition, deviation from linearity is also observed with in-plane transverse loading but the degree of nonlinearity is not comparable to that observed with the in-plane shear [41,42]. Therefore, appropriate modeling of the nonlinear behavior of FRP becomes crucial.

In this investigation, proper constitutive models are introduced to simulate the nonlinear behavior of steel reinforcing bar, prestressing tendon, concrete and FRP. In order to demonstrate the capability and generality of these proposed material models suitable to model the behaviors of reinforced concrete and prestressed concrete structures strengthened by FRP, a series of numerical analyses are carried out by using the finite element program Abaqus [43] and are compared with the experimental results.

2. Material properties and constitutive models

The materials used in the analysis involve steel reinforcing bars, prestressing tendon, concrete and fiber-reinforced plastics. Reliable constitutive models applicable to steel reinforcing bars, prestressing tendon and concrete are available in the Abaqus material library. Thus, their input material properties and associated constitutive models are briefly discussed. The Abaqus program does not have a nonlinear material library for FRP. Hence, its nonlinear constitutive model is discussed here in detail. The resulting nonlinear constitutive equations for the FRP are coded in FORTRAN language as a subroutine and linked to the Abaqus program.

2.1. Steel reinforcing bar

The elastic modulus of the steel reinforcement used in the analyses is assumed to be

$$E_S = 200\ \text{GPa} \tag{1}$$

The stress-strain curve of the reinforcing bar is assumed to be elastic perfectly plastic as shown in Fig. 1.

2.2 Prestressing Tendon

Unless specified, the elastic modulus of the prestressing tendon used in the analyses is also assumed to be $E_S = 200$ GPa. Based on the material tested data, the nonlinear stress-stain curve of the tendon can be simplified to a piecewise linear curve and input to Abaqus.

In Abaqus, the prestressing tendon and the steel reinforcement are treated as equivalent uniaxial materials, which are smeared through the element section. In order to properly model the constitutive behaviors of the tendon and the reinforcement, the cross sectional area, spacing, position and orientation of each layer of tendon or steel bar within each element need to be specified.

2.2. Concrete

The Poisson's ratio ν_C of concrete under uniaxial compressive stress ranges from 0.15 to 0.22, with a representative value of 0.19 or 0.20 [34]. In this study, the Poisson's ratio of concrete is assumed to be

$$\nu_C = 0.2 \quad (2)$$

Let the uniaxial compressive strength and the corresponding strain of the concrete be f_C' and ε_C'. The value of ε_C' is usually around the range of 0.002 to 0.003. A representative value suggested by ACI Committee 318 [44] and used in the analysis is

$$\varepsilon_O = 0.003 \quad (3)$$

The uniaxial tensile strength f_t' of concrete is difficult to measure. For this study the value is taken as [34]

$$f_t' = 0.33\sqrt{f_C'} \text{ MPa} \quad (4)$$

The initial modulus of elasticity of concrete E_C is highly correlated to its compressive strength and can be calculated with reasonable accuracy from the empirical equation [44]

$$E_C = 4700\sqrt{f_C'} \text{ MPa} \quad (5)$$

Under multiaxial combinations of loading, the failure strengths of concrete are different from those observed under uniaxial condition. However, the maximum strength envelope under multiple stress conditions seems to be largely independent of load path [45]. In Abaqus, a Mohr-Coulomb type compression surface together with a crack detection surface is used to model the failure surface of concrete (Fig. 2). When the principal stress components of concrete are in biaxial compression zone, the response of the concrete is modeled by an elastic-plastic theory with an associated flow and an isotropic hardening rule. When the principal stress components of concrete are in biaxial tension zone or in biaxial tension-compression zone, cracking of concrete is defined to occur by the crack detection surface. Once cracking of concrete takes place, the orientation of the crack is stored. Damaged elasticity is then used to model the existing crack [43].

When plastic deformation occurs, there should be a certain parameter to guide the expansion of the yield surface. A commonly used approach is to relate the multidimensional stress and strain conditions to a pair of quantities, namely, the effective stress σ_C and effective strain ε_C, such that results obtained following different loading paths can all be correlated by means of the equivalent uniaxial stress-strain curve. The stress-strain relationship proposed by Saenz [46] has been widely adopted as the uniaxial stress-strain curve for concrete and it has the following form

$$\sigma_C = \frac{E_C \varepsilon_C}{1+(R+R_E-2)(\frac{\varepsilon_C}{\varepsilon_O})-(2R-1)(\frac{\varepsilon_C}{\varepsilon_O})^2+R(\frac{\varepsilon_C}{\varepsilon_O})^3} \quad (6)$$

where

$$R = \frac{R_E(R_\sigma - 1)}{(R_\varepsilon - 1)^2} - \frac{1}{R_\varepsilon}, \quad R_E = \frac{E_C}{E_O}, \quad E_O = \frac{f_C'}{\varepsilon_O}$$

and $R_\sigma = 4$, $R_\varepsilon = 4$ may be used [38]. In the analysis, equation (6) is taken as the equivalent uniaxial stress-strain curve for concrete and approximated by several piecewise linear segments inputted to Abaqus.

When cracking of concrete takes place, a smeared model is used to represent the discontinuous macrocrack behavior. It is known that the cracked concrete of a reinforced concrete element can still carry some tensile stress in the direction normal to the crack, which is termed tension stiffening [34]. In this study, a simple descending line is used to model this tension stiffening phenomenon (Fig. 3). The default value of the strain ε^* at which the tension stiffening stress reduced to zero is [43]

$$\varepsilon^* = 0.001 \quad (7)$$

During the postcracking stage, the cracked reinforced concrete can still transfer shear forces through aggregate interlock or shear friction, which is termed shear retention. Assuming that the shear modulus of intact concrete is G_C, then the reduced shear modulus $\hat{G}$ of cracked concrete can be expressed as

$$\hat{G} = \mu G_C \quad (8)$$

$$\mu = (1 - \varepsilon/\varepsilon_{max}) \quad (9)$$

where ε is the strain normal to the crack direction and ε_{max} is the strain at which the parameter μ reduces to zero (Fig. 4). Numerous analytical results have demonstrated that the particular value chosen for μ (between 0 and 1) does not appear to be critical but values greater than zero are necessary to prevent numerical instabilities [34, 39]. In Abaqus, ε_{max} is usually assumed to be a very large value, i.e., $\mu = 1$ (full shear retention). In this investigation, the default values for tension stiffening parameter $\varepsilon^* = 0.001$ and for shear retention parameter $\mu = 1$ are used.

2.3. Fiber-reinforced plastics

For fiber-reinforced plastics (Fig. 5), each lamina can be considered as an orthotropic layer in a plane stress condition. It is well known that unidirectional fibrous composites exhibit severe nonlinearity in their in-plane shear stress-strain relation. In addition, deviation from linearity is also observed with in-plane transverse loading but the degree of nonlinearity is not comparable to that in the in-plane shear [41]. Usually, this nonlinearity associated with the transverse loading can be ignored [42]. To model the nonlinear in-plane shear behavior, the nonlinear strain-stress relation for a composite lamina suggested by Hahn and Tsai [41] is adopted as follows:

$$\begin{Bmatrix} \varepsilon_1 \\ \varepsilon_2 \\ \gamma_{12} \end{Bmatrix} = \begin{bmatrix} \frac{1}{E_{11}} & -\frac{\nu_{21}}{E_{22}} & 0 \\ -\frac{\nu_{12}}{E_{11}} & \frac{1}{E_{22}} & 0 \\ 0 & 0 & \frac{1}{G_{12}} \end{bmatrix} \begin{Bmatrix} \sigma_1 \\ \sigma_2 \\ \tau_{12} \end{Bmatrix} + S_{6666}\tau_{12}^2 \begin{Bmatrix} 0 \\ 0 \\ \tau_{12} \end{Bmatrix} \quad (10)$$

In this model only one constant S_{6666} is required to account for the in-plane shear nonlinearity. The value of S_{6666} can be determined by a curve fit to various off-axis tension test data [41]. Let us define $\Delta\{\sigma'\} = \Delta\{\sigma_1, \sigma_2, \tau_{12}\}^T$ and $\Delta\{\varepsilon'\} = \Delta\{\varepsilon_1, \varepsilon_2, \gamma_{12}\}^T$. Inverting and differentiating Eq. (10), the incremental stress-strain relations are established

$$\Delta\{\sigma'\} = [Q_1']\Delta\{\varepsilon'\} \quad (11)$$

$$[Q_1^{'}]=\begin{bmatrix} \frac{E_{11}}{1-\nu_{12}\nu_{21}} & \frac{\nu_{12}E_{22}}{1-\nu_{12}\nu_{21}} & 0 \\ \frac{\nu_{21}E_{11}}{1-\nu_{12}\nu_{21}} & \frac{E_{22}}{1-\nu_{12}\nu_{21}} & 0 \\ 0 & 0 & \frac{1}{1/G_{12}+3S_{6666}\tau_{12}^2} \end{bmatrix} \quad (12)$$

Furthermore, it is assumed that the transverse shear stresses always behave linearly and do not affect the nonlinear behavior of any in-plane shear. If we define $\Delta\{\tau_t^{'}\}=\Delta\{\tau_{13},\tau_{23}\}^T$ and $\Delta\{\gamma_t^{'}\}=\Delta\{\gamma_{13},\gamma_{23}\}^T$, the constitutive equations for transverse shear stresses become

$$\Delta\{\tau_t^{'}\}=[Q_2^{'}]\Delta\{\gamma_t^{'}\} \quad (13)$$

$$[Q_2^{'}]=\begin{bmatrix} \alpha_1 G_{13} & 0 \\ 0 & \alpha_2 G_{23} \end{bmatrix} \quad (14)$$

where α_1 and α_2 are the shear correction factors and are taken to be 0.83 in this study.

Among existing failure criteria, the Tsai-Wu criterion [47] has been extensively used in the literature and is adopted in this analysis. Under plane stress conditions, this failure criterion has the following form

$$F_1\sigma_1+F_2\sigma_2+F_{11}\sigma_1^2+2F_{12}\sigma_1\sigma_2+F_{22}\sigma_2^2+F_{66}\tau_{12}^2=1 \quad (15)$$

with

$$F_1=\frac{1}{\bar{X}}+\frac{1}{\bar{X}'},\quad F_2=\frac{1}{\bar{Y}}+\frac{1}{\bar{Y}'},\quad F_{11}=\frac{-1}{\bar{X}\bar{X}'},$$

$$F_{22}=\frac{-1}{\bar{Y}\bar{Y}'},\quad F_{66}=\frac{1}{\bar{S}^2}.$$

The $\bar{X}$, $\bar{Y}$ and $\bar{X}'$, $\bar{Y}'$ are the lamina longitudinal and transverse strengths in tension and compression, respectively, and $\bar{S}$ is the shear strength of the lamina. Though the stress interaction term F_{12} in Eq. (15) is difficult to be determined, it has been suggested that F_{12} can be set equal to zero for practical engineering applications [48]. Therefore, $F_{12}=0$ is used in this investigation.

During the numerical calculation, incremental loading is applied to composite plates until failures in one or more of individual plies are indicated according to Eq. (15). Since the Tsai-Wu criterion does not distinguish failure modes, the following two rules are used to determine whether the ply failure is caused by resin fracture or fiber breakage [49]:

(1) If a ply fails but the stress in the fiber direction remains less than the uniaxial strength of the lamina in the fiber direction, i.e. $\bar{X}'<\sigma_1<\bar{X}$, the ply failure is assumed to be resin induced. Consequently, the laminate loses its capability to support transverse and shear stresses, but remains to carry longitudinal stress. In this case, the constitutive matrix of the lamina becomes

$$[Q_1^{'}]=\begin{bmatrix} E_{11} & 0 & 0 \\ 0 & 0 & 0 \\ 0 & 0 & 0 \end{bmatrix} \quad (16)$$

(2) If a ply fails with σ_1 exceeding the uniaxial strength of the lamina, the ply failure is caused by the fiber breakage and a total ply rupture is assumed. In this case, the constitutive matrix of the lamina becomes

$$[Q_1^{'}]=\begin{bmatrix} 0 & 0 & 0 \\ 0 & 0 & 0 \\ 0 & 0 & 0 \end{bmatrix} \quad (17)$$

During a finite element analysis, the constitutive matrix of composite materials at the integration points of shell elements must be calculated before the stiffness matrices are assembled from the element level to the structural level. For composite materials, the incremental constitutive equations of a lamina in the element coordinates (x,y,z) can be written as:

$$\Delta\{\sigma\}=[Q_1]\Delta\{\varepsilon\} \quad (18)$$

$$\Delta\{\tau_t\}=[Q_2]\Delta\{\gamma_t\} \quad (19)$$

where $\Delta\{\sigma\}=\Delta\{\sigma_x,\sigma_y,\tau_{xy}\}^T$, $\Delta\{\tau\}=\Delta\{\tau_{xz},\tau_{yz}\}^T$, $\Delta\{\varepsilon\}=\Delta\{\varepsilon_x,\varepsilon_y,\gamma_{xy}\}^T$, $\Delta\{\gamma\}=\Delta\{\gamma_{xz},\gamma_{yz}\}^T$, and

$$[Q_1]=[T_1]^T[Q_1^{'}][T_1] \quad (20)$$

$$[Q_2]=[T_2]^T[Q_2^{'}][T_2] \quad (21)$$

$$[T_1]=\begin{bmatrix} \cos^2\theta & \sin^2\theta & \sin\theta\cos\theta \\ \sin^2\theta & \cos^2\theta & -\sin\theta\cos\theta \\ -2\sin\theta\cos\theta & 2\sin\theta\cos\theta & \cos^2\theta-\sin^2\theta \end{bmatrix} \quad (22)$$

$$[T_2]=\begin{bmatrix} \cos\theta & \sin\theta \\ -\sin\theta & \cos\theta \end{bmatrix} \quad (23)$$

The θ is measured counterclockwise from the element local x-axis to the material 1-axis (Fig. 5). Let $\Delta\{\varepsilon\}_O=\Delta\{\varepsilon_{xo},\varepsilon_{yo},\varepsilon_{xyo}\}^T$ be the incremental in-plane strains at the mid-surface of the shell section and $\Delta\{\kappa\}=\Delta\{\kappa_x,\kappa_y,\kappa_{xy}\}^T$ the incremental curvatures. The incremental inplane strains at a distance z from the mid-surface of the shell section become

$$\Delta\{\varepsilon\}=\Delta\{\varepsilon_O\}+z\Delta\{\kappa\} \quad (24)$$

Let h be the total thickness of the composite shell section, the incremental stress resultants, $\Delta\{N\}=\Delta\{N_x,N_y,N_{xy}\}^T$, $\Delta\{M\}=\Delta\{M_x,M_y,M_{xy}\}^T$ and $\Delta\{V\}=\Delta\{V_x,V_y\}^T$ can be defined as:

$$\begin{Bmatrix}\Delta\{N\}\\ \Delta\{M\}\\ \Delta\{V\}\end{Bmatrix}=\int_{-h/2}^{h/2}\begin{Bmatrix}\Delta\{\sigma\}\\ z\Delta\{\sigma\}\\ \Delta\{\tau_t\}\end{Bmatrix}dz \quad (25)$$

Substituting Eqs. (18), (19) and (24) into the above expression, one can obtain the stiffness matrix for the fiber composite laminate shell at the integration point as

$$\begin{Bmatrix}\Delta\{N\}\\ \Delta\{M\}\\ \Delta\{V\}\end{Bmatrix}=\int_{-h/2}^{h/2}\begin{bmatrix}[Q_1] & z[Q_1] & [0]\\ z[Q_1] & z^2[Q_1] & [0]\\ [0]^T & [0]^T & [Q_2]\end{bmatrix}\begin{Bmatrix}\Delta\{\varepsilon_O\}\\ \Delta\{\kappa\}\\ \Delta\{\gamma_t\}\end{Bmatrix}dz \quad (26)$$

where [0] is a 3 by 2 null matrix.

3. Numerical analysis

The validity of the material models for steel, FRP and reinforced concrete has been verified individually by testing against experimental data [43,50] and is not duplicated here. The validity of these material models to simulate the behavior of prestressed concrete, reinforced concrete strengthened by FRP and prestressed concrete strengthened by FRP are demonstrated in this section.

3.1 Axially loaded prestressed concrete columns

To evaluate the ability of the proposed material responses in modeling the prestressed concrete structures, the best starting point is to test them against structures that are subjected to uniform compressive forces. For this purpose, the experimental work of Durrani and Elias [51] is chosen.

The dimensions of the prestressed concrete columns are shown in Fig. 6. The uniaxial compressive strength of the concrete is $f'_c = 38$ MPa. The columns have four prestressing steel wires and each steel wire has a diameter of 5 mm. The stress-strain relation of the wire is shown in Fig. 7. While the specimens A11 and A12 do not have lateral reinforcement, the spacing of the steel lateral reinforcement of the specimens B2 and B3 are given in Table 1. The steel lateral reinforcement has a diameter of 6 mm and a yield stress $f_y = 620$ MPa. The prestress applied to each specimen is also given in Table 1. These specimens are fixed at one end and subjected to axial compressive force at the other end up to failure.

Due to symmetry, only 1/8 portion of the specimen (the shaded part in Fig. 6) is analyzed and symmetric boundary conditions are placed along the symmetric planes. In the finite element analysis, 8-node plane stress elements with reduced integration rule and with 1×10 mesh (1 row in y-direction and 10 rows in z-direction) are used to model the prestressed concrete columns. The Figs. 8 and 9 show the axial stress versus axial strain curves for all the four specimens. It can be seen that the proposed material models are satisfactory in modeling the compressive behavior of the prestressed concrete columns subjected to various prestressing forces and with various lateral reinforcement spacing. Generally, the calculated ultimate strengths are in good agreement with the experiment results (Table 1).

3.2 Laterally loaded prestressed concrete beam

In this example, a prestressed I beam tested by Rabczuk and Eibl [52] are studied. The dimensions of the beam can be found in Fig. 10. The uniaxial compressive strength of the concrete is $f'_c = 45$ MPa. The beam has two tension wires of 12 mm diameter at the lower flange. Each wire was prestressed with a force of 80 KN. The diameter of the upper reinforcement is 10 mm. The stress-strain relation of the wire is shown in Fig. 11. After the prestressed forces are applied, the beam is subjected to four-point static load up to failure.

Due to symmetry, only 1/4 portion of the specimen is analyzed and symmetric boundary conditions are placed along the symmetric planes. In the finite element analysis, 8-node plane stress elements with reduced integration rule and with 21×5 mesh (21 row in x-direction and 5 rows in y-direction) are used to model the prestressed concrete beam. The Fig. 12 shows the lateral load P versus vertical displacement u at the midspan of the beam. It can be seen that the proposed material models are satisfactory in modeling the flexural behavior of the prestressed concrete beam subjected to lateral loading. The calculated ultimate load $P_u = 121$ kN is also in good agreement with the experiment result $P_u = 120$ kN.

3.3 Laterally loaded reinforced concrete beam strengthened by FRP

The validity of the proposed material models to simulate the composite behavior of reinforced concrete beam strengthened by FRP is examined in this section by comparing with the result of beam experiment performed by Shahawy et al. [11]. The dimensions of the test beam are given in Fig. 13. The beam is subjected to four-point static load up to failure. The flexural reinforcement is composed of two 13 mm diameter steel bars in tension zone and two 3 mm diameter steel bars in compression zone. The yielding strength σ_y of the reinforcing steel is 468.8 MPa and the compressive strength f'_c of concrete is 41.37 MPa.

The beams were strengthened with either 2 or 3 layers of FRP adhered to the bottom face of the beam with their fiber directions oriented in the axial direction of the beam. Each FRP layer is 0.17 mm in thickness with tensile strength $\bar{X} = 2758$ MPa and modulus $E_{11} = 141.3$ GPa. To take the Tsai-Wu criterion into account, the following parameters are assumed: $\bar{X} = \bar{Y} = -27.58$ MPa, $\bar{Y} = \bar{S} = 27.58$ MPa, $E_{22} = G_{12} = 1413$ MPa, $S_{6666} = 7.32(\text{GPa})^{-3}$, $\nu_{12} = 0.21$. Since the FRP layers are subjected to uniaxial tension in fiber direction only, these assumed parameters would not affect the uniaxial tensile behavior of the FRP.

The beams have two planes of symmetry. Due to symmetry, only 1/4 portion of the beam is analyzed and symmetric boundary conditions are placed along the two symmetric planes. In the finite element analysis, 8-node solid elements with reduced integration rule are used to model the reinforced concrete beams. The mesh of the beam has 78 solid elements in total (26 rows in x-direction, 3 rows in y-direction and 1 row in z-direction). Because the fiber-reinforced plastics are relatively thin compared to the concrete beam, they are modeled by the 4-node shell elements with reduced integration rule. The FRP shell elements are attached to the bottom surface of the beam directly and perfect bonding between FRP and the concrete is assumed.

Figure 14 shows the moment versus deflection curves of the beam at the midspan. It can be observed that the correlations are quite good between the numerical results and the experimental data. For beam strengthened by 2 FRP layers, the predicted ultimate moment 54.3 kN-m is in good agreement with the experimental ultimate moment 52.2 kN-m. The error is about 4.0%. For beam strengthened by 3 FRP layers, the predicted ultimate moment 60.9 kN-m is also in good agreement with the experimental ultimate moment 60.4 kN-m. The error is only 0.8%.

3.4 Laterally loaded reinforced concrete one-way slabs strengthened by FRP

In this example, two reinforced concrete one-way slabs strengthened by FRP and tested by Seim et al. [17] are studied. The dimensions of the slab can be found in

Fig. 15. The distance from the extreme compression face to the centroid of the longitudinal tension reinforcement was 83 mm. In the longitudinal direction, the reinforcement consisted of three #3 rebars (9.5 mm diameter), whereas twenty three #2 rebars (6.4 mm diameter) at 100 mm spacing were placed in the transverse direction. The yielding strength σ_y of the reinforcing steel is 462 MPa and the compressive strength f_c' of concrete is 33.2 MPa.

Each slab was strengthened with 2 FRP strips adhered to the bottom face of the slab with their fiber directions oriented in the longitudinal direction (Fig. 15). Two different lengths of strip, i.e. L = 1830 mm (full length) or 1460 mm (median length), were used. Each FRP strip is 1.19 mm in thickness with tensile strength $\bar{X}=2270$ MPa and modulus $E_{11}=198$ GPa. In addition, the following parameters are assumed: $\nu_{12}=0.21$, $\bar{X}=\bar{Y}=-22.7$ MPa, $\bar{Y}=\bar{S}=22.7$ MPa, $E_{22}=G_{12}=1980$ MPa, $S_{6666}=7.32(\text{GPa})^{-3}$.

The slabs have two planes of symmetry. Due to symmetry, only 1/4 portion of the slab is analyzed and symmetric boundary conditions are placed along the two symmetric planes. In the finite element analysis, 8-node shell elements with reduced integration rule are used to model the reinforced concrete slabs. In the finite element mesh, there are 27 reinforced concrete shell elements in total (9 rows in the longitudinal direction, 3 rows in the transverse direction). The fiber-reinforced plastics are also modeled by the 8-node shell elements with reduced integration rule and perfect bonding between FRP and the slab is assumed. For slab with strip of full length, 7 FRP shell elements are used. For slab with strip of median length, 6 FRP shell elements are employed. In the experiment, when the slabs failed, the longitudinal strain in the FRP strips is measured and is equal to 0.0065. This maximum strain criterion, i.e. $\varepsilon_1 \le 0.0065$, is used together with the Tsai-Wu criterion for FRP in this numerical analysis.

Figure 16 shows the lateral load P versus vertical displacement u at the midspan of the slabs. It can be observed that the correlation is quite good between the numerical result and the experimental data. For slab strengthened by FRP strips of median length, the predicted ultimate load 41.8 kN is in good agreement with the experimental ultimate load 41.9 kN. The error is only 0.2%. For slab strengthened by FRP strips of full length, the predicted ultimate load 41.5 kN is also in good agreement with the experimental ultimate load 42.5 kN. The error is about 2.4%. The ultimate loads of these two strengthened slabs are very close. This indicates that the use of FRP strips of full length to strengthen the slab may not be necessary.

3.5 Laterally loaded reinforced concrete two-way slabs strengthened by FRP

In this example, two square reinforced concrete two-way slabs tested by Mosallam and Mosalam [20] are studied. The clear span of the two-way slabs in both directions was 264 cm with constant thickness of 76.2 mm as shown in Fig. 17. The slabs are simply supported at the four edges and are subjected to a uniform static pressure applied to the bottom surface of the slabs up to failure. The compressive strength f_c' of concrete is 41.37 MPa. Both reinforced concrete slabs were fabricated using Grade 60 reinforcing steel with the yielding strength σ_y equal to 414 MPa. Tension (top) reinforcement consisted of #3 rebars (9.5 mm diameter) at 305 mm equal spacing in the two orthogonal directions of each slab with 13 mm cover. While one specimen is purely reinforced concrete slab, the other specimen is strengthened by two FRP layers spaced at 457 mm and adhered to the top side with their fiber directions oriented in the two orthogonal directions of the slab (Fig. 17). At the intersection regions of the staggered unidirection laminates, a bidirectional fiber architecture, i.e. [90/0/90/0] lamination layup, was formed. Each FRP layer is 0.58 mm in thickness with tensile strength $\bar{X}=1246$ MPa and modulus $E_{11}=104$ GPa. In addition, the following parameters are assumed: $\nu_{12}=0.3$, $\bar{X}=-1246$ MPa, $\bar{Y}=187$ MPa, $\bar{Y}=-93$ MPa, $\bar{S}=93$ MPa, $E_{22}=6.75$ GPa, $G_{12}=7.1$ GPa, $S_{6666}=7.32(\text{GPa})^{-3}$.

The slabs have two planes of symmetry. Due to symmetry, only 1/4 portion of the slab is analyzed and symmetric boundary conditions are placed along the two symmetric planes. In the finite element analysis, 8-node shell elements with reduced integration rule are used to model the reinforced concrete slabs. In the finite element mesh, there are 25 reinforced concrete shell elements in total (5 rows in each FRP strip direction). The fiber-reinforced plastics are also modeled by the 8-node shell elements with reduced integration rule and perfect bonding between FRP and the slab is assumed. For slab strengthened with FRP strips, 21 FRP shell elements are used.

Figure 18a shows the total lateral force versus vertical displacement at the midspan of the reinforced concrete two-way slab without strengthened by FRP. It can be observed that the correlation is quite good between the numerical result and the experimental data. The predicted ultimate load 217 kN is in good agreement with the experimental ultimate load 219 kN with an error of 0.9%. This again verifies the validity of the proposed material models to model the behavior of reinforced concrete structures.

Figure 18b shows the total lateral force versus vertical displacement at the midspan of the reinforced concrete two-way slab strengthened by FRP. It can be observed that the correlation is also quite good between the numerical result and the experimental data. The predicted ultimate load 394 kN is in good agreement with the experimental ultimate load 404 kN with an error of 2.5%. This again verifies the validity of the proposed material models to model the behavior of reinforced concrete structures strengthened by FRP.

Comparing Fig. 18b with Fig. 18a, we can find that the ultimate load of the slab is significantly increased by about 84%, which proves the usefulness of FRP to strengthen reinforced concrete structures.

3.6 Laterally loaded prestressed concrete solid slabs strengthened by FRP

In this example, prestressed concrete solid slab tested by Shahawy et al. [10] is studied. The test setup for the solid slab is shown in Fig. 19. The compressive strength f_C of the concrete is 41.37 MPa. The pretensioned solid slab has 16 low relaxation strands and the diameter of each strand is 13 mm. The ultimate strength of the prestressing steel is 1862 MPa and the jacking force in each strand is maintained at 138 kN. The elastic modulus of the prestressing strands is assumed to be $E_S = 190$ GPa and the assumed stress-strain relation of the strand is shown in Fig. 20. The FRP layer is 0.17 mm in thickness with tensile strength $\overline{X} = 2758$ MPa and modulus $E_{11} = 141.3$ GPa. In addition, the following parameters, are assumed: $\overline{Y} = \overline{S} = 27.5$ MPa, $\overline{X}' = \overline{Y}' = -27.5$ MPa, $E_{22} = G_{12} = 1413$ MPa, $S_{6666} = 0$, $\nu_{12} = 0.21$.

In the experiment, the prestressed concrete slab is simply supported at two ends (Fig. 19). The slab is subjected to four-point static loading up to its ultimate capacity and unloaded. Then, three FRP layers are bonded to the tension face of the slab. After a complete cure of the adhesive, the retrofitted slab is tested again under four-point loading. Since the retrofitted concrete slab is precracked, the compressive strength of the precracked concrete should be smaller than that of the intact concrete. Therefore, $f_C' = 35$ MPa with a 15% reduction [53] is used in the numerical analysis.

The slab has two planes of symmetry. Therefore, only 1/4 portion of the slab is analyzed and symmetric boundary conditions are placed along the two symmetric planes. In the finite element analysis, 8-node solid elements with reduced integration rule are used to model the prestressed concrete slabs. In the finite element mesh, there are 54 solid elements in total (9 rows in x direction, 3 rows in y direction, 2 rows in z direction).

Figure 21 shows the moment verse deflection curves of the retrofitted prestressed concrete solid slab at the loading points. It can be observed that the correlation is quite good between the numerical result and the experimental data. The predicted ultimate load 519 kN-m is in good agreement with the experimental ultimate load 530 kN-m with an error of 2.1%. This verifies the validity of the proposed material models to model the behavior of prestressed concrete structures strengthened by FRP.

4. Conclusions

As a conclusion, the good agreement obtained in these sets of examples between the numerical predictions and the experimental results establishes the validity and accuracy of using the proposed nonlinear constitutive models for steel reinforcing bars, prestressing tendons, concrete and fiber-reinforced plastics in modeling the behavior of reinforced concrete structures, prestressed concrete structures, reinforced concrete structures strengthened by fiber reinforced plastics and prestressed concrete structures strengthened by fiber reinforced plastics.

5. References

[1] Baker AA. Fiber composite repair of cracked metallic aircraft components - practical and basic aspects. Composite 1987;18(4):293-308.

[2] Ong CL, Chu RC, Ko TC, Shen SB. Composite patch reinforcement of cracked aircraft upper longeron: analysis and specimen simulation. Theoretical and Applied Fracture Mechanics 1990;14(1):13-26.

[3] Naboulsi S, Mall S. Modeling of a cracked metallic structure with bonded composite patch using the three layer technique. Composite Structures 1996;35(3):295-308.

[4] Schubbe JJ, Mall S. Investigation of a cracked thick aluminum panel repaired with a bonded composite patch. Engineering Fracture Mechanics 1999;63(3):305-323.

[5] Ritchie PA, Thomas DA, Lu LW, Connelly GM. External reinforcement of concrete beams using fiber reinforced plastics. ACI Structural Journal 1991;88(4):490-500.

[6] Saadatmanesh H, Ehsani MR. (1991), RC beams strengthened with FRP plates II: analysis and parametric study. Journal of Structural Engineering (ASCE) 1991;117(11):3434-3455.

[7] Nanni A. Flexural behavior and design of RC members using FRP reinforcement. Journal of Structural Engineering (ASCE) 1993;119(11):3344-3359.

[8] Sharif A, Al-Sulaimani GJ, Basunbul IA, Baluch MH, Ghaleb BN. Strengthening of initially loaded reinforced concrete beams using FRP plates. ACI Structural Journal 1994;91(2):160-167.

[9] Chajes MJ, Januszka TF, Mertz DR, Thomson TA, Finch WW. Shear strengthening of reinforced concrete beams using externally applied composite fabrics. ACI Structural Journal 1995;92(3):295-303.

[10] Shahawy MA, Beitelman T, Arockiasamy M, Sowrirajan R. Experimental investigation on structural repair and strengthening of damaged prestressed concrete slabs utilizing externally bonded carbon laminates. Composites Part B: Engineering 1996;27(3-4):217-224.

[11] Shahawy MA, Arockiasamy M, Beitelman T, Sowrirajan R. Reinforced concrete rectangular beams strengthened with CFRP laminates. Composites Part B: Engineering 1996;27(3-4):225-233.

[12] Chambers RE. ASCE design standard for pultruded Fiber-Reinforced-Plastic (FRP) structures. Journal of Composites for Construction (ASCE) 1997;1(1):26-38.

[13] Malek AM, Saadatmanesh H. Analytical study of reinforced concrete beams strengthened with web-bonded fiber reinforced plastic plates or fabrics. ACI Structural Journal 1998;95(3):343-352.

[14] Mukhopadhyaya P, Swamy N, Lynsdale C. Optimizing structural response of beams strengthened with GFRP plates. Journal of Composites for Construction (ASCE) 1998;2(2):87-95.

[15] Tedesco JW, Stallings JM, El-Mihilmy, M. Finite

element method analysis of a concrete bridge repaired with fiber reinforced plastic laminates. Computers and Structures 1999;72(1-3):379-407.
[16] Vecchio FJ, Bucci F. Analysis of repaired reinforced concrete structures. Journal of Structural Engineering (ASCE) 1999;125(6):644-652.
[17] Seim W, Hörman M, Karbhari V, Seible F. External FRP poststrengthening of scaled concrete slabs. Journal of Composites for Construction 2001;5(2):67-75.
[18] Teng JG, Chen JF, Smith ST, Lam, L. FRP Strengthened RC Structures, John Wiley & Sons, Inc., 2002.
[19] Chaallal O, Shahawy M, Hassan M. Performance of axially loaded short rectangular columns strengthened with carbon fiber reinforced polymer wrapping. Journal of Composite for Construction 2003;7(3):200-208.
[20] Mosallam AS, Mosalam KM. Strengthening of two-way concrete slabs with FRP composites laminates. Construction and Building Materials 2003;17(1):43-54.
[21] Ebead U, Marzouk H. Fiber-reinforced polymer strengthening of two-way slabs. ACI Structural Journal 2004;101(5):650-659.
[22] Vougioukas E, Zeris CA, Kotsovos MD. Toward safe and efficient use of fiber-reinforced polymer for repair and strengthening of reinforced concrete structures. ACI Structural Journal 2005;102(4):525-534.
[23] Pellegrino C, Modena C. Fiber-reinforced polymer shear strengthening of reinforced concrete beams: experimental study and analytical modeling. ACI Structural Journal 2006;103(5):720-728.
[24] Jing M, Raongjant W, Li ZX. Torsional strengthening of reinforced concrete box beams using carbon fiber reinforced polymer. Composite Structures 2007;78(2):264-270.
[25] Petrou MF, Parler D, Harries KA, Rizos DC. Strengthening of reinforced concrete bridge decks using carbon fiber-reinforced polymer composite materials. Journal of Bridge Engineering 2008;13(5):455-467.
[26] El-Tawil S, Okeil AM. LRFD flexural provisions for prestressed concrete bridge girders strengthened with carbon fiber-reinforced polymer laminates. ACI Structural Journal 2002;99(2):181-190.
[27] Hassan T, Rizkalla S. Flexural strengthening of prestressed bridge slabs with FRP systems. PCI Journal 2002;47(1):76-93.
[28] Wu ZS, Iwashita K, Hayashi K, Higuchi T, Murakami S, Koseki Y. Strengthening prestressed-concrete girders with externally prestressed PBO fiber reinforced polymer sheets. Journal of Reinforced Plastics and Composites 2003;22(14):1269-1286.
[29] Larson KH, Peterman RJ, Rasheed HA. Strength-fatigue behavior of fiber reinforced polymer strengthened prestressed concrete T-beams. Journal of Composites for Construction 2005;9(4):313-326.
[30] Lee DC, Karbhari VM. Rehabilitation of large diameter prestressed cylinder concrete pipe (PCCP) with FRP composites - Experimental investigation. Advances in Structural Engineering 2005;8(1):31-44.
[31] Huang PC, Nanni A. Dapped-end strengthening of full-scale prestressed double tee beams with FRP composites. Advances in Structural Engineering 2006;9(2):293-308.
[32] Rosenboom O, Rizkalla S. Behavior of prestressed concrete strengthened with various CFRP systems subjected to fatigue loading. Journal of Composites for Construction 2006;10(6):492-502.
[33] Kim YJ, Shi C, Green MF. Ductility and cracking behavior of prestressed concrete beams strengthened with prestressed CFRP sheets. Journal of Composites for Construction 2008;12(3):274-283.
[34] ASCE Task Committee on Concrete and Masonry Structure. State of the art report on finite element analysis of reinforced concrete, ASCE, 1982.
[35] Chen WF. Plasticity in reinforced concrete, McGraw-Hill, 1982.
[36] Meyer C, Okamura H. Finite element analysis of reinforced concrete structures, ASCE, 1985.
[37] Vecchio FJ, Collins MP. The modified compression-field theory for reinforced concrete elements subjected to shear. ACI Journal 1986;83(2):219-231.
[38] Hu H-T, Schnobrich WC. Constitutive modelling of concrete by using nonassociated plasticity. Journal of Materials in Civil Engineering (ASCE) 1989;1(4):199-216.
[39] Hu H-T, Schnobrich WC. Nonlinear analysis of cracked reinforced concrete. ACI Structural Journal 1990;87(2):199-207.
[40] Hu H-T, and Schnobrich WC. Nonlinear finite element analysis of reinforced concrete plates and shells under monotonic loading. Computers and Structures 1991;38(5/6):637-651.
[41] Hahn HT, Tsai SW. Nonlinear elastic behavior of unidirectional composite laminae. Journal of Composite Materials 1973;7(1):102-118.
[42] Jones RM, Morgan HS. Analysis of nonlinear stress-strain behavior of fiber-reinforced composite materials. AIAA Journal 1977;15(12):1669-1676.
[43] Abaqus, Inc., Abaqus Analysis User's Manuals and Example Problems Manuals, Version 6.8 Providence, Rhode Island, 2008.
[44] ACI Committee 318. Building Code Requirements for Structural Concrete and Commentary (ACI 318-08), American Concrete Institute, Detroit, Michigan, 2008.
[45] Kupfer H, Hilsdorf HK, Rusch H. Behavior of concrete under biaxial stresses. ACI Journal 1969;66(8):656-666.
[46] Saenz LP. Discussion of "Equation for the stress-strain curve of concrete" by Desayi P and Krishnan S. ACI Journal 1964;61(9):1229-1235.
[47] Tsai SW, Wu, EM. A general theory of strength for anisotropic materials. Journal of Composite Materials 1971;5(1):58-80.
[48] Narayanaswami R, Adelman HM. Evaluation of the tensor polynomial and Hoffman strength theories

for composite materials. Journal of Composite Materials 1977;11(4):366-377.
[49] Rowlands RE. Strength (failure) theories and their experimental correlation. in Failure Mechanics of Composites, Edited by Sih GC and Skudra AM, Elsevier Science Publishers, The Netherlands, 1985, pp. 71-125.
[50] Lin W-P, Hu H-T. Nonlinear analysis of fiber-reinforced composite laminates subjected to uniaxial tensile load. Journal of Composite Materials 2002;36(12):1429-1450.
[51] Durrani AJ, Elias HE. Confinement of prestressed concrete columns. Journal Prestressed Concrete Institute 1988;33(3):122-141.
[52] Rabczuk T, Eibl J. Numerical analysis of prestressed concrete beams using a coupled element free Galerkin/finite element approach. International Journal of Solids and Structures 2004;41(3-4):1061-1080.
[53] Hognestad E. A Study of Combined Bending and Axial Load in Reinforced Concrete Members. University of Illinois Engineering Experimental Station, Bulletin Series No.399, November, 1951, pp. 128.

Table 1 Prestress, lateral reinforcement and ultimate load for Durrani-Elias specimens

Spec.	Prestress (MPa)	Spacing of Lateral Rein. (mm)	Ultimate Load (MPa)		
			Exp.	Num.	Error (%)
A11	930	none	36.7	36.4	0.82
A12	770	none	33.2	33.7	1.51
B2	770	51	38.6	37.9	1.81
B3	770	75	37.2	38.2	2.59

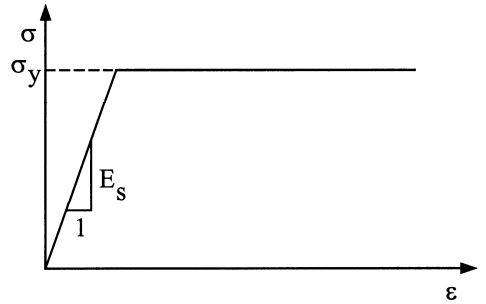

Fig. 1 Elastic perfectly plastic model for steel reinforcing bar

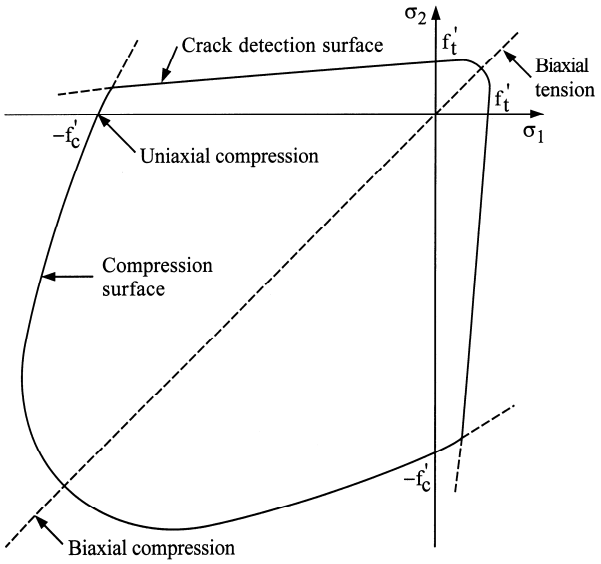

Fig. 2 Concrete failure surface in plane stress

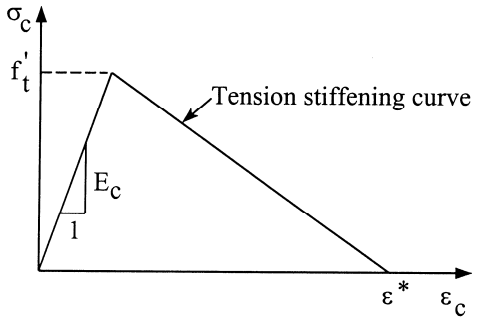

Fig. 3 Tension stiffening model

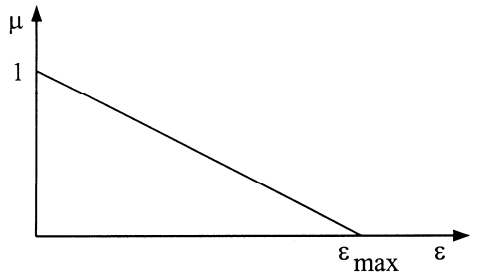

Fig. 4 Shear retention parameter

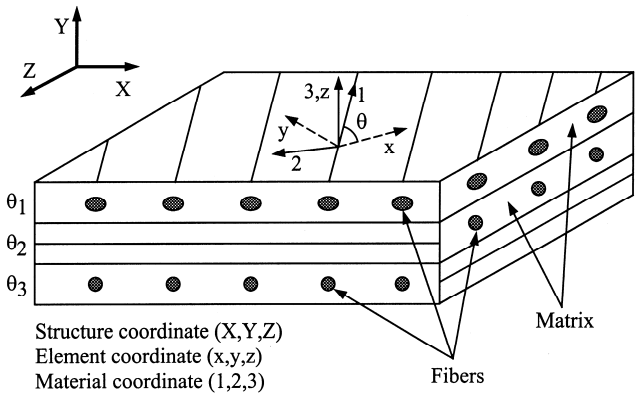

Fig. 5 Material, element and structure coordinates of fiber reinforced plastics

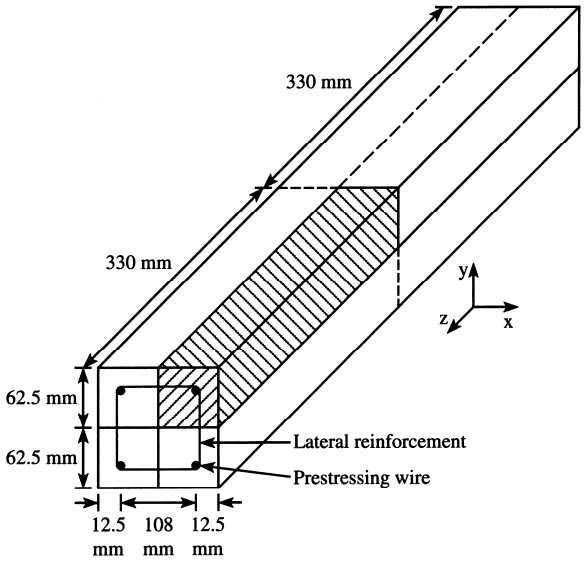

Fig. 6 Durrani-Elias specimens for prestressed concrete columns

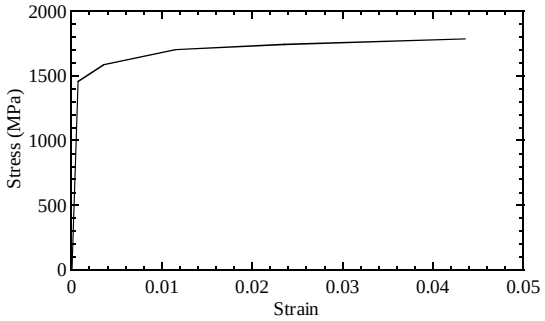

Fig. 7 Stress-strain relation of prestressing steel wire for Durrani-Elias specimens

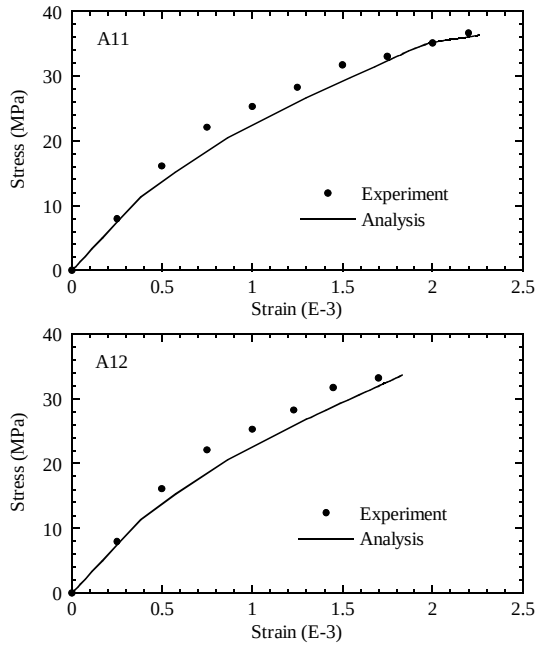

Fig. 8 Stress–strain curves of prestressed concrete columns without lateral reinforcement

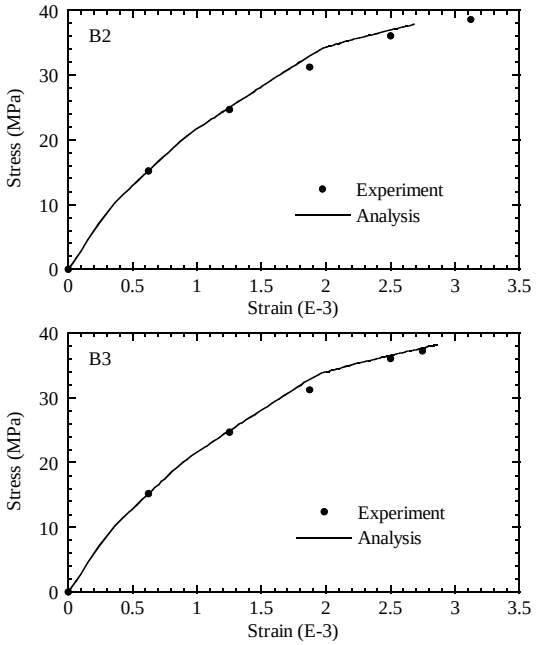

Fig. 9 Stress–strain curves of prestressed concrete columns with lateral reinforcement

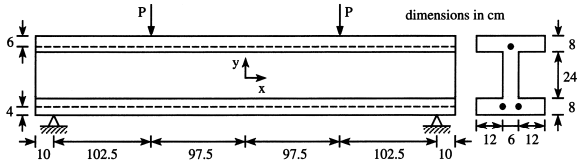

Fig. 10 Rabczuk-Eibl specimen for prestressed concrete beam

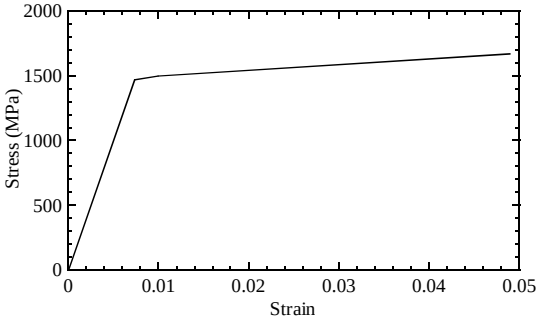

Fig. 11 Stress-strain relation of steel wire for Rabczuk-Eibl specimen

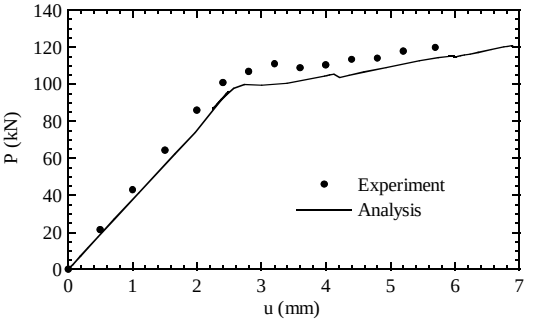

Fig. 12 Load–deflection curves of prestressed concrete beam

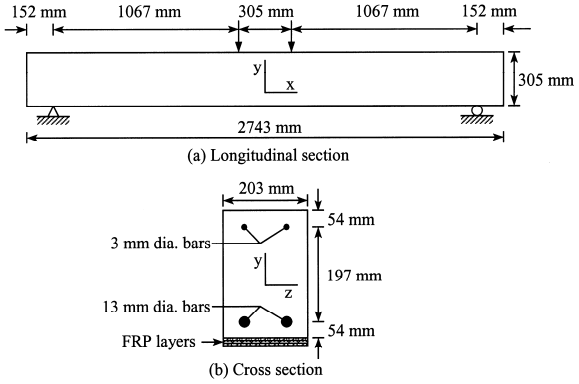

Fig. 13 Shahawy et al. specimens for reinforced concrete beams

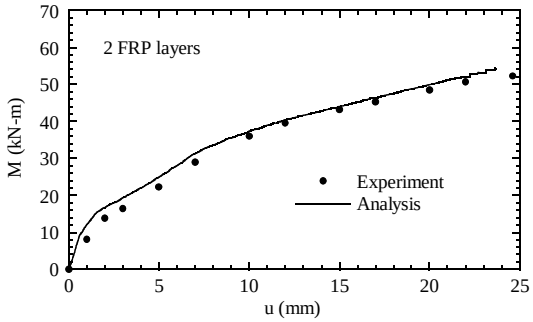

(a) Reinforced concrete beams strengthened by 2 FRP layers

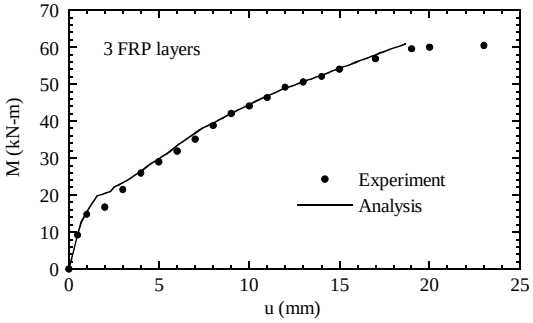

(b) Reinforced concrete beams strengthened by 3 FRP layers

Fig. 14 Moment–deflection curves of reinforced concrete beams strengthened by various FRP layers

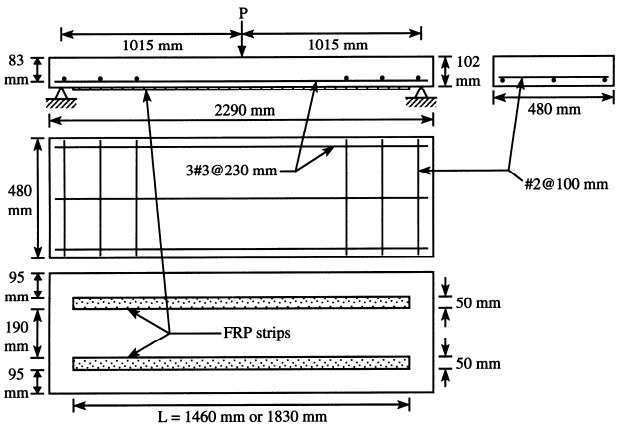

Fig. 15 Seim et al. specimens for reinforced concrete one-way slabs

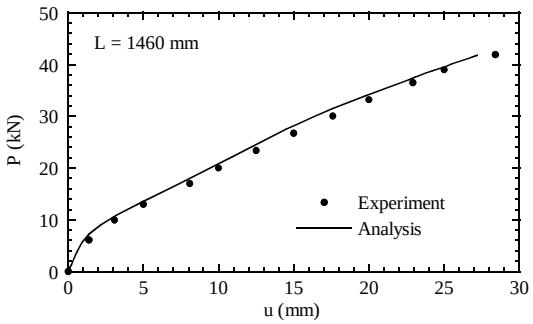

(a) Reinforced concrete one-way slab strengthened by FRP of median length

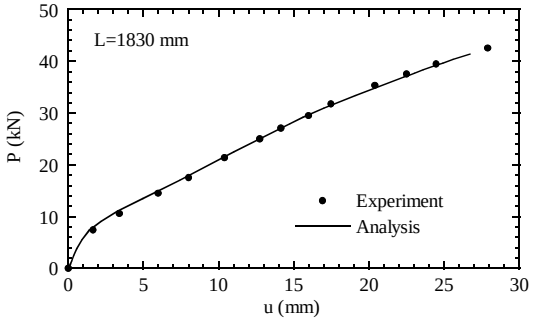

(b) Reinforced concrete one-way slab strengthened by FRP of full length

Fig. 16 Load–deflection curves of reinforced concrete one-way slabs strengthened by various lengths of FRP strips

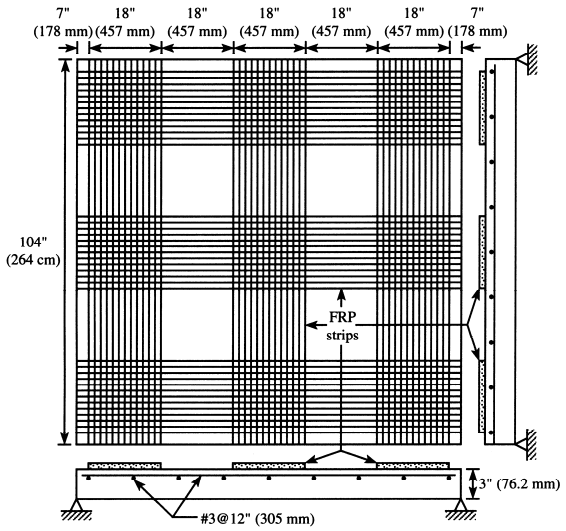

Fig. 17 Mosallam-Mosalam specimens for reinforced concrete two-way slabs

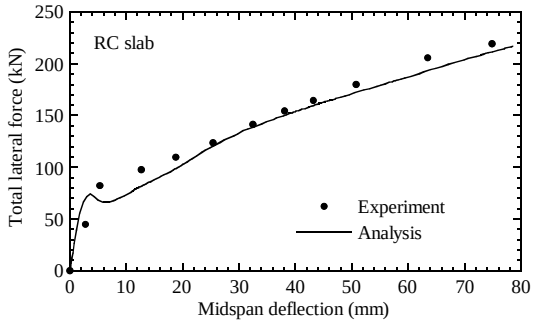

(a) Reinforced concrete two-way slab without FRP

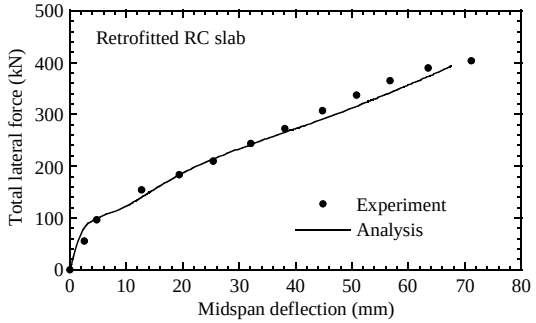

(b) Reinforced concrete two-way slab with FRP

Fig. 18 Load–deflection curves of reinforced concrete two-way slabs with or without FRP

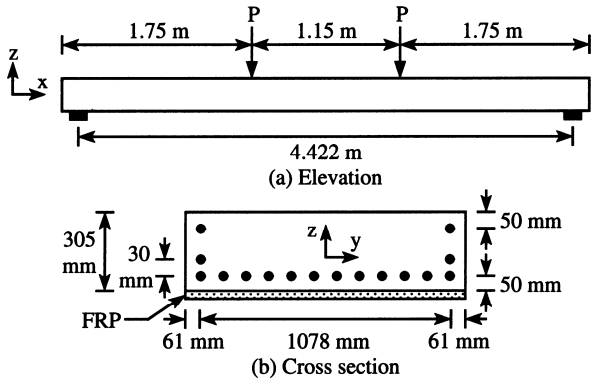

Fig. 19 Shahawy et al. specimens for prestressed concrete solid slabs

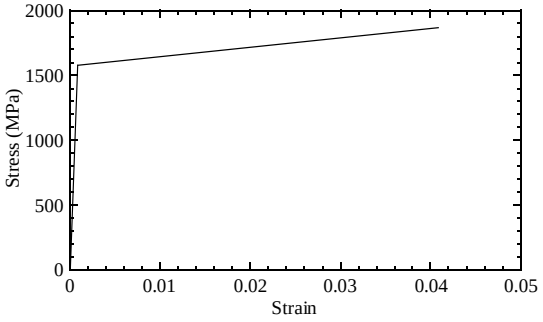

Fig. 20 Stress-strain relation of prestressing steel strand for Shahawy et al. specimens

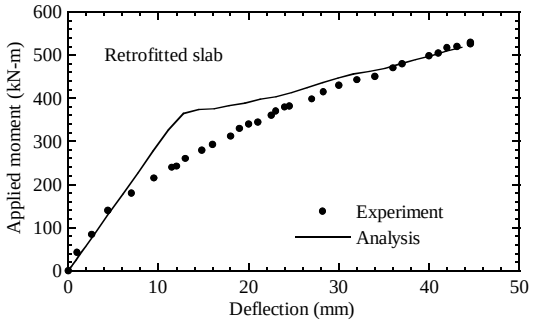

Fig. 21 Moment–deflection curves of prestressed concrete solid slabs strengthened by FRP at loading points